ADVANCED INTELLIGENT SYSTEMS
Open Access
www.advintellsyst.com

Combining Deep Learning and Compressed Sensing Methods for the 3D Characterization of Ultra-Thin Epitaxial Layers Grown on Controlled-Shape Nano-Oxides

*Justyna Grzonka, José Marqueses-Rodríguez, Susana Fernández-García, Xiaowei Chen, José J. Calvino, and Miguel López-Haro**

Using a nanostructured platform (a controlled-shape nano-oxide) and conventional wet impregnation techniques, powder-type materials have been prepared in which atomically thin surface layers are deposited under very mild conditions. More importantly, an advanced methodology, combining energy dispersive X-ray spectroscopy-scanning transmission electron tomography (STEM-EDX ET) and deep learning denoising techniques, has been developed for the 3D compositional characterization of these unique nanosystems. The complex case of LaO_x-coated CeO_2 nanocubes is illustrated. For these, aberration corrected 2D STEM-EDX evidence that ceria nanocubes become covered with a 2–4 atom-thick layer of a La, Ce-mixed oxide with spatially varying composition. However, STEM-EDX ET reveals that this layer distributes unevenly, patching most of the available nanocube surface. The large flexibility and spread availability of the involved synthetic techniques enables, using the tools here developed, a wide exploration of the wealth of questions and applications of these intriguing, atomically thin, surface oxide phases.

1. Introduction

The field of 2D nanophases, with single to a few atomic layer thicknesses, is attracting increasing interest and expanding from just graphene[1–3] based materials to include a richer variety of compounds, such as metallic dichalcogenides[4–6] (WS_2, MoS_2, and diselenides[7–9]), 3*d* metal oxides, noble metals (Au) or the so-called 2D-Xenes from group 14 (Silicenes, Germanenes, Stanenes), group 15 (Phosphorenes) and, more recently, MXenes (with M a 3*d* metal). Both the development of huge surface areas and the occurrence of large modifications in electronic properties, due to quantum confinement effects, combined with the varied intrinsic properties of the bulk materials, support expectations of fruitful applications in fields such as catalysis, optics, electronics, magnetism or energy conversion and storage.

The layered structure of the corresponding bulk phases allows in some cases preparing these 2D phases, as freestanding materials, by exfoliation or using much more complex methods like liquid phase epitaxy, molecular beam epitaxy, chemical vapor deposition, metal–organic chemical vapor deposition, atomic or pulsed layer deposition or magnetron sputtering deposition. For those cases in which the bulk phase depicts highly isotropic symmetries, as can be the case of the f.c.c. noble metal lattices, synthetic approaches have exploited the template effect or the use of capping agents in solution.

In the field of catalysis, dominated from a practical point of view by the use of a high surface area, powder type, substrates, atomic layer deposition (ALD) has been assayed to deposit, in a controlled way, conformal, thin, metal, and oxide films.[10,11] Encouraging results have been recently reported in $Pd/ZrO_2/CeO_2$,[12] $Pd/CeO_2/Al_2O_3$[13] and $Pd/Fe_2O_3/Al_2O_3$[14] systems prepared by means of ALD, which showed improvements in activity and stability. Although these works point out a definite influence of epitaxial growth also in the case of high surface area substrates, ALD still relies on nonconventional preparation equipment and complex precursors of the thin film components.

Nevertheless, the development of very robust and reproducible synthesis methods for controlled-shape nano-oxides provides, in our view, an interesting alternative for epitaxial growth, using much more conventional, widely available, routes. These nanomaterials occupy an intermediate position between low surface area single-crystals, of common use in surface science, and the high surface area powders employed in industrial catalysis. Their potential as models to rationalize the influence of surface chemistry on a variety of chemical and catalytic processes (CO oxidation, water gas shift, and preferential oxidation of CO

J. Grzonka, J. Marqueses-Rodríguez, S. Fernández-García, X. Chen, J. J. Calvino, M. López-Haro
Departamento de Ciencias de los Materiales e Ingeniería Metalúrgica y Química Inorgánica
Facultad de Ciencias
Universidad de Cadiz
Campus Rio San Pedro S/N, Puerto Real, 11510 Cádiz, Spain
E-mail: miguel.lopezharo@uca.es

The ORCID identification number(s) for the author(s) of this article can be found under https://doi.org/10.1002/aisy.202200231.

DOI: 10.1002/aisy.202200231

in hydrogen) is being exploited in an increasing number of studies.

Note that most of the nanosized crystallites in these oxides depict flat, extended, surfaces with well-defined crystallographic structure; i.e., as in macroscopic single-crystals but at the nanoscale. Since the principles underlying epitaxial growth should hold at this scale, we hypothesized that conformal thin films could be grown on these substrates using wet impregnation and calcinations at mild temperatures (<500 °C); an easy and routine technique to prepare supported catalysts.

Fernandez-Garcia et al.[15] have demonstrated that 10% La-modified ceria nanocubes present improved redox properties and an enhancement of their hydroxyl radicals scavenging activity. They have reported that the excellent properties shown by these new nanomaterials are related to a La-enriched surface. This surface segregation of La was further confirmed by Collins et al.[16] through the application of model-based tomography spectra.

Following these results, it appears that controlling the nature of the surface by depositing a continuous layer of La over pure ceria shape-controlled nanocubes would allow tuning both the redox and other surface properties of these systems.

To retrieve information about the structure and spatial distribution of the elements in materials with this type of architecture, 2D STEM images or elemental maps using either energy-dispersive x-ray spectroscopy (EDX) or electron energy loss spectroscopy (EELS) are commonly employed. However, due to the chemical fluctuations which can occur on the surface of the crystallites along the direction of the incoming electron beam, analytical studies in 2D projection are insufficient. Moreover, as it will be shown here, the 2D analysis leads to the loss or misinterpretation of some relevant details, even when performed on aberration corrected equipment. In fact, retrieval of the exact morphology and actual extent of the ultrathin surface layer, unavoidably requires 3D information. This is a key piece of information, since it determines the homo or heterogeneous chemical nature of the exposed surface.

Currently, scanning transmission electron tomography,[17,18] combined with EDX[19–25] or EELS,[16,22,26,27] provides 3D compositional information. However, to avoid beam damage effects, these techniques involve the use of a limited number of projection images and a reduction of the electron dose,[28,29] particularly in the case of STEM-EDX tomography. Regarding the limited number of projections, efficient reconstruction algorithms are needed to avoid the well-known missing wedge. In this regard, compressed sensing (CS) has been demonstrated as very promising to obtain elemental distributions in 3D.[22]

The last limitation enforces the application of digital post-processing techniques which allow for enhancing the quality of the raw EDX spectrum images while preserving the information. Among the techniques to improve the raw 2D EDX maps, we can highlight those based on denoising through filtering,[30] including blur filters that smear out the signal among close pixels and which are included in the commercially available software for electron microscopes. Other possibilities arise from most sophisticated methodologies based on a multivariate statistical analysis of the spectroscopic dataset[31,32] or deep learning techniques, which have been recently applied for experimental data of Zn/S/Se quantum dots,[33] gold nanorods[33] and Au–Ag nanoparticle structures.[34]

Bringing together the two aspects commented earlier, in this article, we intend to solve a complex challenge: the 3D compositional characterization of nanostructured catalysts based on a heavy functional oxide, CeO_2 ($Z_{Ce} = 58$) modified at the very first surface layers with La ($Z_{La} = 57$) oxide using STEM-EDX. Apart from those intrinsically related to the analytical technique, the difficulties, in this case, arise from: 1) the very close value of the atomic number of the elements involved, which precludes their discrimination by high-angle annular dark field (HAADF) imaging; 2) the limited thickness of the surface layer, in the order of the nanometer; 3) the low molar content of La in the material, around 10%; 4) the cubic-type shape of the nanocrystals, hard to reconstruct due to their quite low sphericity.

We have tackled these difficulties by combing 2D and 3D analytical experiments at the nm-scale using EDX. The raw EDX elemental maps used to reconstruct the volume of the La signal were digitally post-processed using deep learning techniques and reconstructed using algorithms based on compressed sensing. The results were compared with reconstructions denoised with a Gaussian blur filter, and in-painting methods as well as using simply raw data. Finally, the importance of a joint and complementary 2D EDX analysis and EDX electron tomography approach to reliably solve such complex characterization challenges will be highlighted.

2. Results and Discussion

In **Figure 1**a, a representative atomic resolution HAADF-STEM image of 10%LaO_x–CeO_2 nanocube prepared by wet chemical routes is shown. Digital diffraction pattern (DDP) (inset in Figure 1a) analysis performed from the entire image indicates the characteristic distances and angles of {200} and {220} crystallographic planes of a cubic lattice imaged down the [001] zone axis. Note also from this image the presence of truncations at the corners of cube, which are associated with {110} and {111} facets, whereas the flat facets of the cube correspond to {100} surfaces.[35] This morphology is in good agreement with that already described in the literature[35,36] and therefore no modifications are found after the process of nanomaterials preparation.

Figure 1b displays a magnified HR-HAADF STEM image from the same nanocube. A first inspection from the surface of the cube shows a perfect coherence between the cationic planes located just at the surface and those which correspond to the bulk. This feature can be confirmed by taking an intensity line profile from the green marked arrow and presented in Figure 1c. In any case, the intensities in HAADF-STEM images are related to both the thickness and the atomic number (Z) of the elements present in the sample, however, cerium ($Z_{Ce} = 58$) and lanthanum ($Z_{La} = 57$) are next to each other in the periodic table. Therefore, the differences in contrast observed at the edges of the cube are more likely connected with thickness variations. Thus, a precise determination of the La distribution requires the application of spectroscopic techniques like EDX.

The EDX elemental maps of La–L (green), Ce–L (red) lines, and overlay La–L and Ce–L signal maps are displayed in Figure 1d–f. As expected, the La signal is very weak due to

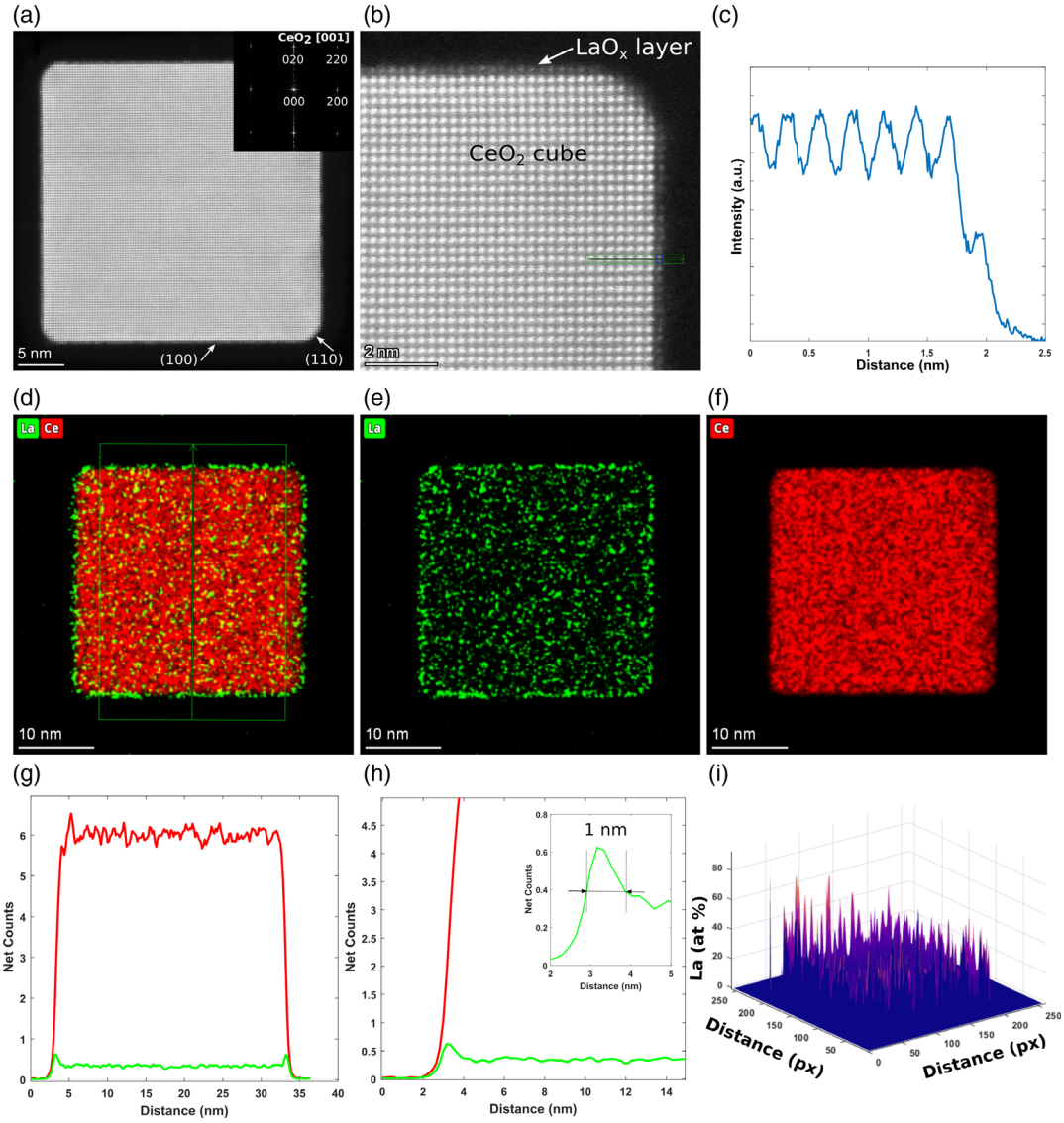

Figure 1. a,b) High-resolution high-angle annular dark field-scanning transmission electron tomography (HR HAADF-STEM) images of a CeO_2 cube covered with atomically thin LaO_x layer acquired down the [001] zone axis. c) Intensity line profile across the interface between the CeO_2 cube and the LaO_x layer at the position marked in *b* with a green arrow. STEM-energy dispersive X-ray spectroscopy (EDX) maps of: d) La + Ce, e) La, and f) Ce after applying a Gaussian blur filter (sigma = 0.8) to enhance the La signal. g) Averaged EDX La and Ce line profiles across the region indicated with a green arrow in (d). h) Magnified left part of the profile revealing the position of the La concentration peak inside that of Ce with thickness measurement of the LaO_x layer (inset). i) Surface representation of La at% distribution over the CeO_2 cube. The La and Ce signals are plotted in green and red, respectively.

the low amount of La used for the preparation of the nanomaterials, see Figure S1 (Supporting Information), however, we can clearly observe that La distributes surrounding the cube, but with some regions of enrichment (see the bottom left part of the cube). The La and Ce averaged profiles (Figure 1g,h) taken from the region indicated with a green arrow in Figure 1d demonstrates that a 1 nm thick La-containing layer is grown on top of the nanocubes.

Such analysis performed on a large number of 10%LaO_x–CeO_2 nanocubes evidence similar features, i.e., a few atoms thick LaO_x layer distributed around the cube (Figure S2, Supporting Information), showing a thickness that varies from 0.8 to 1.7 nm. Thickness measurements were performed using the statistical analysis described in Lopez-Haro et al.[37] Note that this simple incipient wetness impregnation method provides in fact an ultrathin epitaxial layer growth on the nanocubes.

Another important characteristic can be observed from the La and Ce average profiles. In particular, it should be noticed that the La signal distributes inside the Ce signal profile. In fact, the profile analysis performed for most cubes reveals that the La peak locates inward of the Ce profile (Figure S2, Supporting Information). This result suggests an intensive La-diffusion into the CeO_2 nanocrystallite volume during the synthesis. Alternatively, it could be also related to beam broadening which

affects the spatial resolution of STEM-EDX mapping. However, it has been reported that in aberration-corrected microscopes, the spatial resolution in STEM-EDX experiment is better than 1 nm.[38] More localized line profiles, illustrated in Figure S3, Supporting Information, in which only 2 adjacent pixels were averaged for each plot point, clearly show that the La peak shifts from outside to inside the Ce profile. These fluctuations evidence local heterogeneities in the composition of the layer.

A surface plot representation of La atomic percentage obtained after quantifying the La–L and Ce–L signals using the *k*-factors method (Figure 1i) evidence a large fluctuation in the composition of the layer, in the La at% ranging from 5 to 75%. This indicates that heating at 400 °C transforms the La precursor to oxides, intermixing of La and Ce within the first surface layers, giving rise to a $Ce_xLa_yO_{2-\delta}$ mixed oxide layer rather than a pure LaO_x layer.

To determine in larger detail, the La distribution over the CeO_2 nanocubes and the likely mixing between them, a series of simulated EDX maps, corresponding to structural models which considered ceria nanocubes fully coated by a thin surface layer of a Ce–La mixed oxide of varying composition were calculated. **Figure 2** shows: i) the simulated EDX maps, ii) corresponding line profiles taken vertically across the center of the cube and iii) surface plot representations of La in at%. The simulations were performed for cerium cubes completely covered with a Ce–La mixed oxide layer with La molar contents of: a) 100%, b) 80%, c) 60%, d) 40%, and e) 20%, which correspond to 50%, 36%, 25%, 15%, and 7% at. La in the total volume. The models were created in such a way that the La atoms in the layer were randomly replaced, in the proper amount, by Ce atoms to simulate the heterogeneities already observed in the experimental maps. The line profiles extracted from each of the simulated EDX map (Figure 2(ii)) demonstrate that the shift in the position and in the relative intensity of the La peak with respect to the position of the Ce signal correlates with the layer composition. Thus, for 100% La the La peak is placed completely outside the Ce profile. When its content decreases to 80%, the La peak corresponding to the highest content of La at the edges of CeO_2 cubes, starts to shift inside the Ce profile. Further decrease of La content to 60, 40% and 20% lead to a continuous drop in the intensity of the La peak and shift up to a complete location inside the Ce profile.

To quantify the simulated La–L map, the intensities were transformed to counts per second following the equations proposed by MacArthur et al.[39] The surface plot representation of La in at% (Figure 2(iii)) indicates how the concentration of the two lanthanides changes with the decrease of La content from 100 to 20%. Comparison of our experimental results from Figure 1 and S2, Supporting Information, with those obtained by simulation, indicate that the projected La concentration in the LaO_x–CeO_2 mixed oxide layer should be at the level of 20–40%. These values correspond to a total La content in the cubes in the 7–15% range, which is in very good agreement with the loading used to synthesize these nanomaterials. These results confirm that the ultra-thin layer is formed by a $LaCeO_x$ mixed oxide, instead of pure LaO_x.

This composition for the mixed oxide layer falls within the range observed in bulk, solid-solution type, La_2O_3–CeO_2 mixed oxides prepared by co-precipitation methods, for which a maximum solubility of La in CeO_2 of roughly 50% has been reported.[40] Importantly, a chemical interaction between the two lanthanides takes place in this ultra-thin mixed oxide layer, as evidenced by the hydrogen temperature-programmed reduction study (H_2-TRP) included in the Figure S12, Supporting Information. As discussed there, the fine details of the H_2-TPR diagram of the 10% LaO_x–CeO_2 nanocubes agree well with the concentration of lanthanum in the topmost surface layers evidenced by 2D STEM-EDS.

EDX electron tomography studies were performed to get further information about the distribution of the $CeLaO_x$ layer over the CeO_2 cubes. In these experiments, HAADF images and EDX maps are acquired simultaneously for a whole tilt series. To avoid sample damage, the tilt series have been recorded from −70 to 70 every 5° or 10°, using a dwell time of 50 µs. These recording conditions limit the quality of the EDX spectra. Background subtraction and peak deconvolution were applied to the EDX data to separate as much as possible the La and Ce contributions to the signal, since the La–L and Ce–L lines are partially overlapping, as illustrated in Figure S1, Supporting Information. In addition, as a consequence of the low amount of the La precursor used during synthesis a low number of counts is observed for the La signal, which makes its analysis much more complicated.

Recently, Skorikov et al.[34] have demonstrated that the quality of the EDX elemental maps can be improved by denoising them using deep learning methods. Therefore, our aligned raw EDX tilt series for La–L and Ce–L were denoised by using this advanced method, which is described in more detail in the Supporting Information section. **Figure 3** illustrates a qualitative comparison between raw experimental EDX maps for La and Ce with those denoised using a deep learning network (DLN) for the projections acquired at −40° and 40° tilts. It can be observed that after using this method a large improvement in the quality of the signal is obtained with respect to the raw data. Thus, for the Ce signal, a smooth and sharp morphology is retained, while in the case of the La signal the areas depicting La agglomeration are smoothed and, what is more important, the clouds of scattered points surrounding the nanocube were removed in the denoised La elemental map recorded at 0° tilt. These large improvements will allow us to visualize better the distribution of La after reconstructing the volume of Ce and La signals.

To better demonstrate the improvement obtained after applying the DL methodology, **Figure 4** compares the reconstruction obtained from: a) raw data with those obtained after denoising: b) with a Gaussian blur filter, c) an in-painting method, and d) using deep learning. In all cases, the reconstruction step was performed through the application of the TVM3D algorithm. In the reconstructed volumes, Ce and La are visualized in red and green, respectively. Importantly, despite the reconstruction considered, the LaO_x layer is discontinuous and some differences in the extent of the coverage of particular facets are observed. To clearly visualize the distribution of La, orthogonal slices through both Ce and La reconstructions are displayed. Note that the slices obtained from the reconstructions where Gaussian blur and in-painting denoising was applied are not very different from those derived from the raw data reconstruction. In all of them, the La signal extends to locations far inside the bulk of the cube, which is not consistent with the very mild conditions used to synthesize

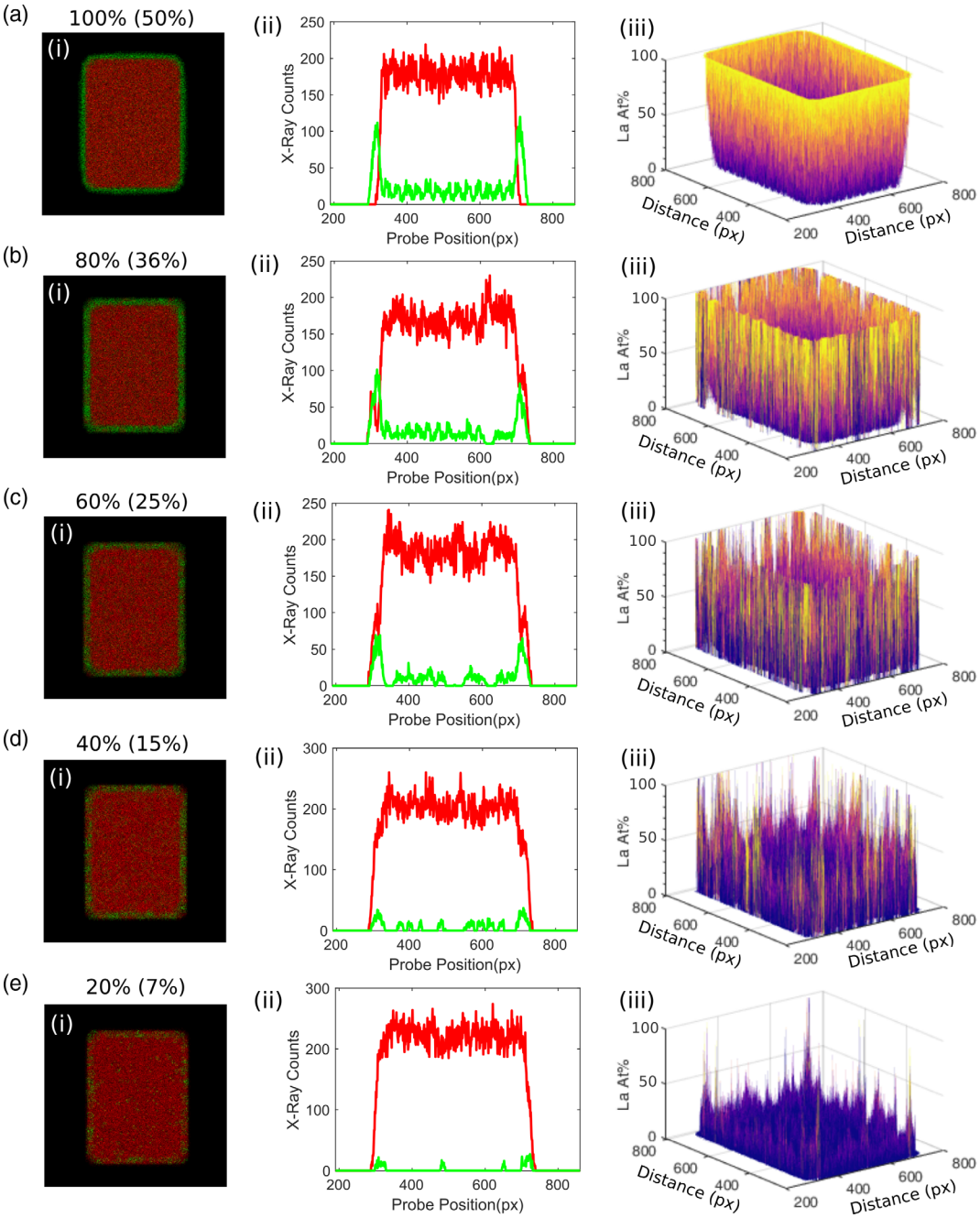

Figure 2. STEM-XEDS simulation study of CeO_2 nanocubes covered by a 1 nm thick LaO_x–CeO_2 layer with: a) 100%, b) 80%, c) 60%, d) 40%, and e) 20% of La in the layer. i) Overlapped La+Ce simulated EDX maps; ii) corresponding averaged line profiles taken vertically across the center of the cube; iii) surface plot of La (at%). In (i) and (ii), the La–L signal is plotted in green, while the Ce–L signal is shown in red. In brackets, the percentage of La in the total volume is shown.

the samples and, therefore, it rather seems a reconstruction artifact. Furthermore, the reconstructed LaO_x layer is much thicker and rougher than expected from the 2D STEM observations. This is very likely due to the fact that to avoid a very noisy final result, the value of the μ hyperparameter required for reconstruction fall in the range which provides a very smoothed and compact signal (Figure S4, Supporting Information).

DLN-based denoising results in a thinner and better-defined layer, particularly for the slices in the *xz* plane (Figure 4d(v)). Furthermore, slices through the *xy* plane (Figure 4d(ii)) match perfectly with the raw EDX map acquired at 0°, Figure S1a, Supporting Information, especially concerning the shape of the La rich region situated in the upper facet of the nanocube. Additionally, it is important to mention that La is partially

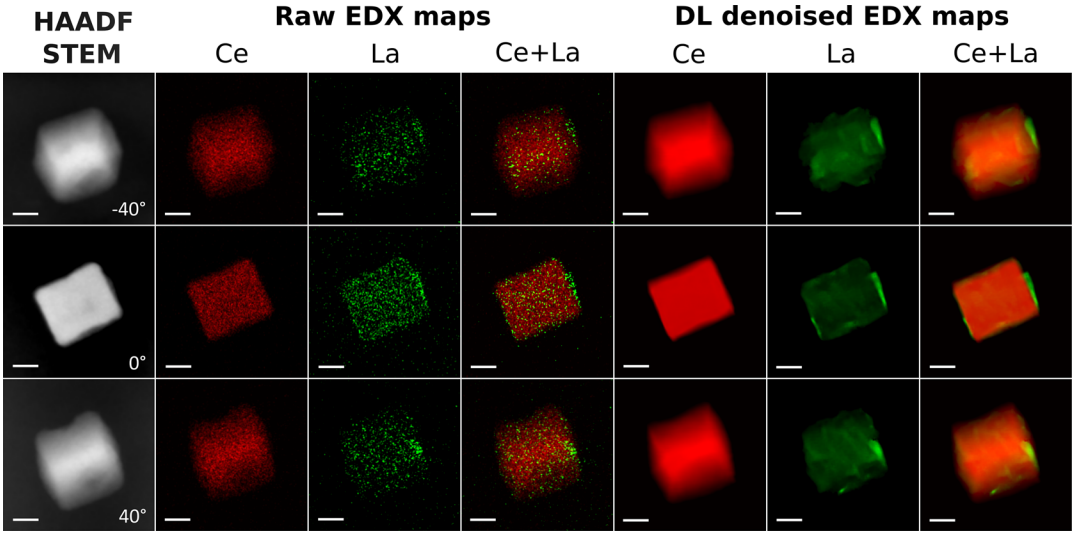

Figure 3. HAADF-STEM images of a LaO_x–CeO_2 nanocube acquired at different tilt angles: −40°, 0°, and 40° with corresponding Ce, La, and Ce + La raw and deep learning (DL) denoised EDX maps used for the reconstruction. The La–L signal is shown in green, while the Ce–L signal is shown in red. The scale bars correspond to 10 nm.

embedded in the Ce signal, which is also in good agreement with the results obtained from the 2D experiments. These results clearly highlight the key role of advanced DLN-based denoising algorithms to reach reliable results, even in cases of severe difficulty as the one considered here, involving an ultra-thin layer epitaxially grown on the surface of a quite chemically close substrate.

After demonstrating that combing DLN methods and CS-based reconstructions allowed us to detect and characterize an ultra-thin La layer, this new methodology was applied to a set of LaO_x–CeO_2 nanocubes to reach an evaluation of La distribution with more statistical significance (Figure S5–S10, Supporting Information). **Figure 5** illustrates additional examples of this study. It shows in particular 3D renderings of the tomographic reconstructions of both La and Ce distributions, in the left column using solid colors and transparent colors in the middle column, and the thickness distribution of the La layer, the right column.

Note that La does not distribute uniformly over the CeO_2 nanocubes but, instead, in a patchy-like pattern, which extends on a fraction of the total available surface. Furthermore, part of the La signal extends inside the nanocube and overlaps to a great extent with the Ce signal, which suggests mixing between La and Ce in the first atomic layers as well as a locally varying La/Ce ratio, in good agreement with the 2D analysis.

The surface of the La and Ce 3D volumes (A_{La} and A_{Ce})can be determined and compared with that of the HAADF-STEM signal reconstruction(A_{HAADF}). By doing this, a value can be determined for the extent of the overlap between La and Ce. Values in the order of 30% were obtained according to the following equation

$$\%\text{La} - \text{Ce overlap} = 100 \times \frac{A_{HAADF} - (A_{La} + A_{Ce})}{A_{HAADF}} \quad (1)$$

Moreover, the ratio between the areas of the two signals (A_{La}/A_{Ce})allows evaluating the degree of coverage of the nanocube surface by the ultrathin mixed oxide layer. Values in the range of 30–70%, with an average of 45% were determined for the experiments shown in Figure 5. As expected, the lowest values are observed, in cases like that of particle 2, where LaO_x accumulates as 3D islands. The largest coverage limit corresponds to a homogeneous distribution of La in the form of a very thin mixed oxide layer. In any case, La does not completely wrap the nanocubes, as the 2D EDX maps suggest, Figure 1 and 2. The analytical ET study clearly reveals that this is just a projection artifact.

If all this quantitative 3D information is taken into account, an average composition of 38% at. La can be estimated for the $CeLaO_x$ surface layer, which is in fact in very good agreement with the results of the 2D analysis.

Regarding the thickness of the La layer, Figure 5(iii) evidences variations over the whole nanocube surface. The highest thickness value, close to 3 nm, corresponds to regions where some agglomeration of La was already detected during the acquisition of 2D EDX maps. Generally, the thickness values detected fall far below that value and agree quite well with that observed in 2D STEM-EDX measurements. In fact, most thickness measurements fall in the 0.8–1.7 nm range.

If the values of total La atomic loading (10%), the size distribution of the nanocubes (Figure S11, Supporting Information) and the surface density of Ce^{4+} ions per square nanometer of {001} type surface of the oxide (6.83 Ce^{4+} nm^{-2}) are taken into account, coverage by a layer containing in average 38% at. La would require a layer thickness of roughly 1.1 nm, which is in the order of magnitude observed here. Of course, decreasing either the %La at. in the layer or the coverage percentage results in an increase of the layer thickness, up to values in the order of 3 nm.

Surface layers with thickness in the same range have been observed on the surface of other ceria nanoshapes. Thus, in a STEM-EELS tomography study of the spatial distribution in

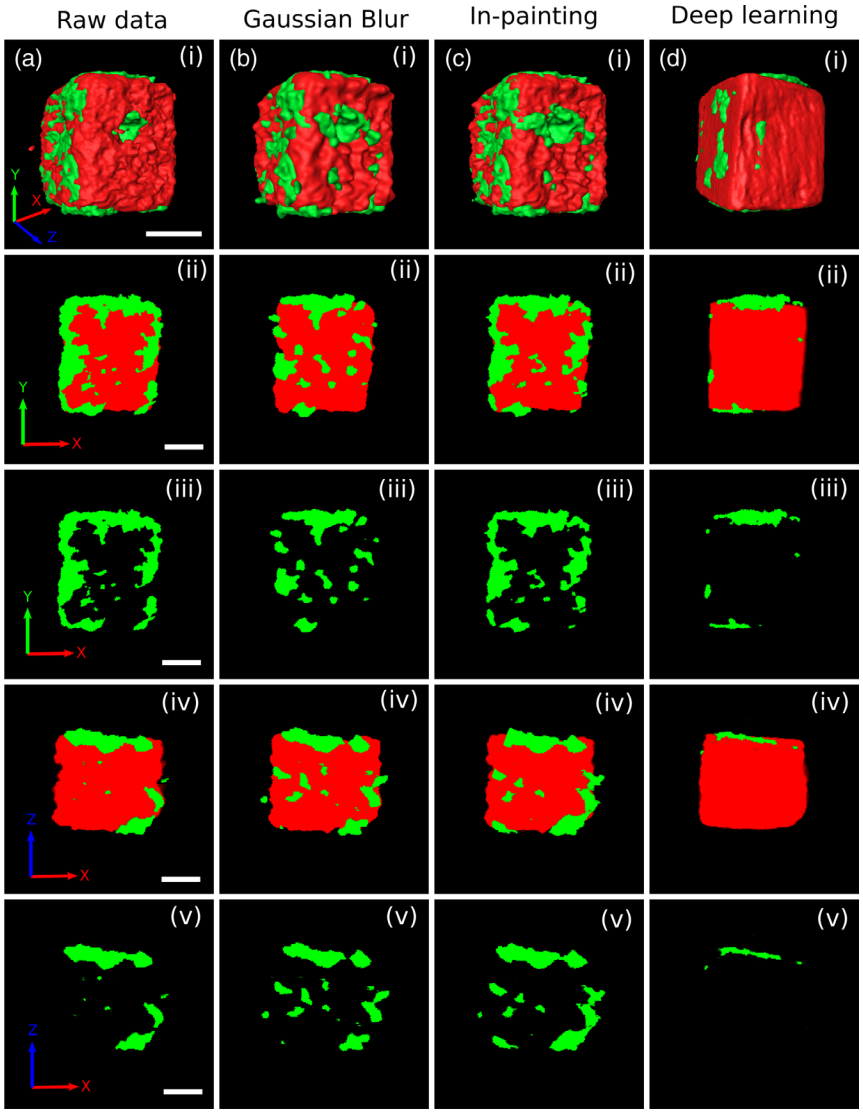

Figure 4. Comparison of TVM3D reconstruction results of a LaO_x–CeO_2 nanocube using: a) raw data, without any processing and data after applying: b) Gaussian blur filter, c) in-painting method, and d) denoising based on DL methodology. i) 3D surface rendering of the tomographic reconstruction; ii–v) EDX electron tomography orthoslices extracted from the entire volume of the reconstructions through *xy* plane for: ii) La+Ce and iii) La distribution and through the *xz* plane for: iv) La + Ce and v) La distribution. The scale bars correspond to 10 nm.

3D of the oxidation states of the lanthanide over the surface of CeO_2 nano-octahedra, with size in the few nanometer range (<15 nm), Goris et al.[27] reported the occurrence of a Ce^{3+} rich (20–50%) surface layer, with thickness in the range of 0.8–1.4 nm, fully covering a Ce^{4+} core. The use of EELS was in that case totally necessary, since differentiation in electronic states is not achievable by means of EDX.

At least the following factors could contribute to the observed limited coverage of the nanocube surfaces: 1) a heterogeneous distribution of the liquid layer of the precursor aqueous solution onto the surface, during the impregnation step; 2) de-wetting of a homogeneous liquid solution layer driven by the strong capillary forces which build up during the drying step; 3) a limited wetting capacity of the mixed oxide, due to the poor structural match between the hexagonal lattice of La_2O_3 and the {100} facets of cubic CeO_2, which depict a square-type arrangement of both Ce and O in consecutive layers stacked along the [001] direction. The last factor may be particularly important at low temperatures, as are those used in the synthesis of the material here investigated, at which diffusion processes are most likely rather limited.

The structural coherency of the two phases at the interface between the ultra-thin surface layer and CeO_2 is largely dependent on the crystallographic nature of the exposed surfaces and, therefore, on the exact morphology of the CeO_2 crystallites. Ag this respect, the comparative structural analysis included in the Supporting Information (Figure S13 and S14) between the structures of La_2O_3 and CeO_2, suggests a potential higher coverage

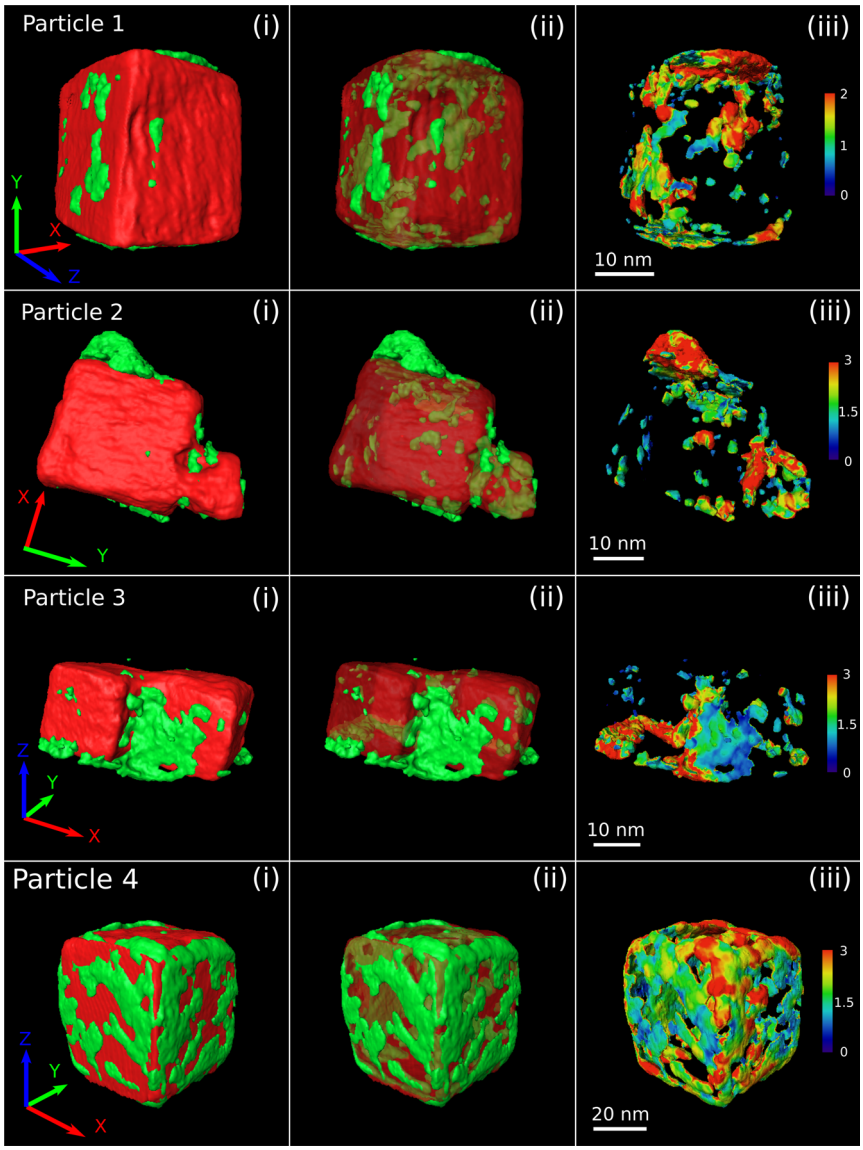

Figure 5. 3D rendered volumes showing the distribution of the LaO_x layer over the CeO_2 cubes. In i,ii) La is shown in green and Ce in red. In (ii) red was set to be transparent to better visualize the distribution of La signal. iii) Thickness distribution of the LaO_x layer. The colormap legend corresponds to thickness in [nm].

degree for ultra-thin La–Ce mixed oxide layers grown on CeO_2 nanocrystallites, whose surface structure is dominated by the contribution of {111} planes.

3. Conclusions

In summary, this study evidences first that only the combination of 2D and 3D analysis can provide the information required to determine with reliability the whole set of relevant structural/compositional features of nanomaterials involving the epitaxial growth of ultrathin layers (with thickness in the nanometer or subnanometer range) and components with close chemistries.

Second, the involvement of advanced deep learning techniques to denoise the raw EDX maps in the tilt series becomes the key to reach 3D reconstructions consistent with the whole set of STEM characterization results.

2D analysis reveals a reliable source of information regarding the atomic structure and thickness of the epitaxial layer, as well as its average composition. However, it entirely fails to provide an accurate picture of the actual spatial distribution of the epitaxial layer over the surface of the underlying substrate, a feature that can only be reliably captured by STEM-EDX tomography.

In the LaO_x–CeO_2 case investigated here, projected 2D EDX maps accurately evidence the formation of a nanometer-thick layer of a mixed La–Ce oxide, with locally varying composition. However, the homogenous coverage of the underlying ceria nanocubes by a continuous layer of this mixed oxide is revealed as a projection artifact by 3D STEM-EDX.

DLN-denoised and CS-reconstructed STEM-EDX tilt series from a set of particles reveal, instead, a partial, patchy-like, coverage of the CeO_2 nanocubes by a mixed oxide layer, 0.8–1.7 nm thick.

Although the proposed methodology still requires further improvements, it provides the best answer, when compared with those obtained from just raw data or after denoising with other approaches, either more conventional ones, like Gaussian filtering, or more advanced, as it is the case of in-painting. The two latter result in a distribution of the outer layer which extends to a large distance into the bulk of the substrate, an artifact of the whole reconstruction process.

The case investigated here explores the limits of complexity, not only due to the proximity in the Periodic Table of the elements involved but also to other relevant questions, such as the very low percentage of the minor component, the small dimensions of one them or the low sphericity of the target objects. Therefore, the proposed methodology is expected to work properly in a wide variety of situations, including other systems with components of similar atomic Z number and application in other fields, like GaSe multilayers, Co–Fe particles, or Au–Pt systems, for which the knowledge about the relative distribution of each of the elements is required to rationalize their synthesis and function.

Finally, regarding the specific materials investigated in this work, the developed methodology will allow considering the influence of both synthetic and structural factors on the details of the final ultra-thin layers. Among them, the morphology of the CeO_2 crystallites, the molar loading of the second lanthanide, the characteristics of the drying step, or the value of the calcination temperature. Work is currently underway to explore these factors.

Supporting Information

Supporting Information is available from the Wiley Online Library or from the author.

Acknowledgements

This work has been co-financed by the Department of Economy, Knowledge, Business and University of the Regional Government of Andalusia, Project references: FEDER-UCA18-107139. Financial support from MCIN/AEI/ 10.13039/501100011033 PID2019-110018GA-I00, PID2020-113006-RB-I00, and PID2020-113809RB-C33 are also acknowledged. Electron microscopy data were acquired using the equipment at the DME-UCA node of the ELECMI Spanish Unique Infrastructure for Electron Microscopy of Materials.

Conflict of Interest

The authors declare no conflict of interest.

Author Contributions

The manuscript was written through the contributions of all authors. All authors have given approval for the final version of the manuscript.

Data Availability Statement

Research data are not shared.

Keywords

compressed sensing, deep learning, electron tomography, energy dispersive X-ray spectroscopy, ultra-thin layers

Received: July 27, 2022
Revised: October 24, 2022
Published online: January 19, 2023

[1] K. S. Novoselov, A. K. Geim, S. V. Morozov, D. Jiang, Y. Zhang, S. V. Dubonos, I. V. Grigorieva, A. A. Firsov, *Science* **2004**, *306*, 666.
[2] K. S. Novoselov, A. K. Geim, S. V. Morozov, D. Jiang, M. I. Katsnelson, I. V. Grigorieva, S. V. Dubonos, A. A. Firsov, *Nature* **2005**, *438*, 197.
[3] Y. Zhang, Y. W. Tan, H. L. Stormer, P. Kim, *Nature* **2005**, *438*, 201.
[4] C. Lee, H. Yan, L. E. Brus, T. F. Heinz, J. Hone, S. Ryu, *ACS Nano* **2010**, *4*, 2695.
[5] C. Ataca, M. Topsakal, E. Aktürk, S. Ciraci, *J. Phys. Chem. C* **2011**, *115*, 16354.
[6] A. Molina-Sánchez, L. Wirtz, *Phys. Rev. B: Condens. Matter Mater. Phys.* **2011**, *84*, 155413.
[7] S. Substrates, X. Lu, M. I. B. Utama, J. Lin, X. Gong, J. Zhang, Y. Zhao, S. T. Pantelides, J. Wang, Z. Dong, Z. Liu, W. Zhou, Q. Xiong, *Nano Lett.* **2014**, *14*, 2419.
[8] A. Ramasubramaniam, *Phys. Rev. B: Condens. Matter Mater. Phys.* **2012**, *86*, 241201.
[9] W. T. Hsu, L. S. Lu, D. Wang, J. K. Huang, M. Y. Li, T. R. Chang, Y. C. Chou, Z. Y. Juang, H. T. Jeng, L. J. Li, W. H. Chang, *Nat. Commun.* **2017**, *8*, 929.
[10] K. Cao, J. Cai, X. Liu, R. Chen, *J. Vac. Sci. Technol., A* **2018**, *36*, 010801.
[11] A. K. Datye, M. Votsmeier, *Nat. Mater.* **2021**, *20*, 1049.
[12] T. M. Onn, L. Arroyo-Ramirez, M. Monai, T. S. Oh, M. Talati, P. Fornasiero, R. J. Gorte, M. M. Khader, *Appl. Catal., B* **2016**, *197*, 280.
[13] T. M. Onn, S. Zhang, L. Arroyo-Ramirez, Y. Xia, C. Wang, X. Pan, G. W. Graham, R. J. Gorte, *Appl. Catal., B* **2017**, *201*, 430.
[14] T. M. Onn, M. Monai, S. Dai, L. Arroyo-Ramirez, S. Zhang, X. Pan, G. W. Graham, P. Fornasiero, R. J. Gorte, *Appl. Catal., A* **2017**, *534*, 70.
[15] S. Fernandez-Garcia, L. Jiang, M. Tinoco, A. B. Hungria, J. Han, G. Blanco, J. J. Calvino, X. Chen, *J. Phys. Chem. C* **2016**, *120*, 1891.
[16] S. M. Collins, S. Fernandez-Garcia, J. J. Calvino, P. A. Midgley, *Sci. Rep.* **2017**, *7*, 5406.
[17] P. A. Midgley, M. Weyland, *Ultramicroscopy* **2003**, *96*, 413.
[18] P. A. Midgley, R. E. Dunin-Borkowski, *Nat. Mater.* **2009**, *8*, 271.
[19] Z. Saghi, X. Xu, Y. Peng, B. Inkson, G. Möbus, *Appl. Phys. Lett.* **2007**, *91*, 251906.
[20] K. Lepinay, F. Lorut, R. Pantel, T. Epicier, *Micron* **2013**, *47*, 43.
[21] B. Goris, L. Polavarapu, S. Bals, G. Van Tendeloo, L. M. Liz-Marzán, *Nano Lett.* **2014**, *14*, 3220.
[22] G. Haberfehlner, A. Orthacker, M. Albu, J. Li, G. Kothleitner, *Nanoscale* **2014**, *6*, 14563.
[23] P. Burdet, Z. Saghi, A. N. Filippin, A. Borrás, P. A. Midgley, *Ultramicroscopy* **2016**, *160*, 118.
[24] T. J. A. Slater, A. Janssen, P. H. C. Camargo, M. G. Burke, N. J. Zaluzec, S. J. Haigh, *Ultramicroscopy* **2016**, *162*, 61.
[25] F. J. R. Mejías, S. Trasobares, M. López-Haro, R. M. Varela, J. M. G. Molinillo, J. J. Calvino, F. A. Macías, *ACS Appl. Mater. Interfaces* **2019**, *11*, 41925.

[26] K. Jarausch, P. Thomas, D. N. Leonard, R. Twesten, C. R. Booth, *Ultramicroscopy* **2009**, *109*, 326.
[27] B. Goris, S. Turner, S. Bals, G. Van Tendeloo, *ACS Nano* **2014**, *8*, 10878.
[28] Z. Saghi, M. Benning, R. Leary, M. Macias-Montero, A. Borras, P. A. Midgley, *Adv. Struct. Chem. Imaging* **2015**, *7*, https://doi.org/10.1186/s40679-015-0007-5.
[29] H. Vanrompay, A. Béché, J. Verbeeck, S. Bals, *Part. Part. Syst. Charact.* **2019**, *36*, 1900096.
[30] P. Potapov, P. Longo, E. Okunishi, *Micron* **2017**, *96*, 29.
[31] P. Potapov, A. Lubk, *Adv. Struct. Chem. Imaging* **2019**, *5*, 4.
[32] N. Mevenkamp, K. E. MacArthur, V. Tileli, P. Ebert, L. J. Allen, B. Berkels, M. Duchamp, *Ultramicroscopy* **2020**, *209*, 112877.
[33] Y. Han, J. Jang, E. Cha, J. Lee, H. Chung, M. Jeong, T. G. Kim, B. G. Chae, H. G. Kim, S. Jun, S. Hwang, E. Lee, J. C. Ye, *Nat. Mach. Intell.* **2021**, *3*, 267.
[34] A. Skorikov, W. Heyvaert, W. Albecht, D. M. Pelt, *Nanoscale* **2021**, *13*, 12242.
[35] M. Tinoco, S. Fernandez-Garcia, M. Lopez-Haro, A. B. Hungria, X. Chen, G. Blanco, J. A. Perez-Omil, S. E. Collins, H. Okuno, J. J. Calvino, *ACS Catal.* **2015**, *5*, 3504.
[36] C. Dong, Y. Zhou, N. Ta, W. Shen, *CrystEngComm* **2020**, *22*, 3033.
[37] M. Lopez-Haro, L. Guétaz, T. Printemps, A. Morin, S. Escribano, P. H. Jouneau, P. Bayle-Guillemaud, F. Chandezon, G. Gebel, *Nat. Commun.* **2014**, *5*, 5229.
[38] M. Watanabe, in *Scanning Transmission Electron Microscopy: Imaging and Analysis*, (Eds: S. J. Pennycook, P. D. Nellist), Springer New York: New York, NY, **2011**; pp 291–351, https://doi.org/10.1007/978-1-4419-7200-2_7.
[39] K. E. MacArthur, M. Heggen, R. E. Dunin-Borkowski, *Adv. Struct. Chem. Imaging* **2018**, *4*, 2.
[40] S. Bernal, G. Blanco, G. Cifredo, J. A. Pérez-Omil, J. M. Pintado, J. M. Rodríguez-Izquierdo, *J. Alloys Compd.* **1997**, *250*, 449.